Applied Catalysis B: Environmental 339 (2023) 123143

Contents lists available at ScienceDirect

Applied Catalysis B: Environmental

journal homepage: www.elsevier.com/locate/apcatb

# Light-assistance in nitrogen fixation to ammonia by highly dispersed Cs-promoted Ru clusters supported on $ZrO_2$

Yong Peng [a], Arianna Melillo [a], Run Shi [b], Amparo Forneli [a], Antonio Franconetti [c], Josep Albero [a,*], Hermenegildo García [a,*]

[a] Departamento de Química/Instituto Universitario de Tecnología Química (CSIC-UPV), Universitat Politècnica de València, Avda. de los Naranjos s/n, 46022 Valencia, Spain

[b] Key Laboratory of Photochemical conversion and Optoelectronic Materials, Technical Institute of Physics and Chemistry, Chinese Academy of Sciences, Beijing 100190, China

[c] Departamento de Química Orgánica, Facultad de Química, Universidad de Sevilla, 41012 Sevilla, Spain

ARTICLE INFO

*Keywords:*
Metal clusters
Photocatalysis
$N_2$ fixation
Ammonia
MOF-derived photocatalyst
Surface plasmonic resonance effects
Hot electrons injection

ABSTRACT

Light-assisted $N_2$ fixation to $NH_3$ under mild conditions is attracting massive attention to circumvent energy crisis and global warming. Herein, highly dispersed Cs-decorated Ru sub-nanometric clusters supported on $ZrO_2$ NPs have been prepared by means of MOF-templated transformation method. The obtained catalyst exhibited $N_2$ hydrogenation activity of 1.6 $mmol_{NH3}$ $g_{cat}^{-1}$ $h^{-1}$ in the dark (350 °C, 0.1 MPa). Remarkably this value increased by over 300 %, reaching 5.1 $mmol_{NH3}$ $g_{cat}^{-1}$ $h^{-1}$ (204 $mmol_{NH3}$ $g_{Ru}^{-1}$ $h^{-1}$) under 1 Sun power illumination (1080 W/$m^2$) The influence of the incident light wavelength has been evaluated, revealing 81 % and 213 % enhancement in the NIR and visible region, respectively. DFT calculations were carried out to understand the static adsorption states of Ru sub-nanoclusters. Mechanistic studies have confirmed the co-existence of a photothermal and a nonthermal-hot electron mechanism. XPS, PXRD and FTIR analysis have determined that the Cs species block surface $Zr^{4+}$ acidity, increasing the basicity of the $ZrO_2$ support. Moreover, partially reduced $Cs^{\delta+}$ ($0 < \delta < 1$) species surrounding the Ru active sites are donating electron density to the adjacent Ru sites, favoring $N_2$ adsorption and subsequent activation. Finally, this photocatalyst has shown an extended stability for 100 h irradiation under continuous flow.

## 1. Introduction

Solar-assisted production of fuels and commodity chemicals, such as methanol, ethylene or ammonia, among others, is becoming increasingly considered as an appealing approach for energy sector decarbonization and climate change mitigation [1]. In this regard, besides the classic photocatalytic mechanism, characterized by the photo-induced generation of electron/hole pairs and their direct participation in red/ox reactions, photothermal catalysis has recently appeared as a very convenient approach due to the higher efficiency [2,3]. The photothermal mechanism consists on light absorption at the active metal sites, which causes an increase of its local temperature at the nanoscale, resulting in an enhanced catalytic activity of the metal sites. For instance, we have recently demonstrated that Cs-promoted Ru clusters supported in a low thermal conductivity support ($SrTiO_3$) is a very convenient photothermal catalyst for $N_2$ hydrogenation at near 1 Sun light irradiation and 350 °C, obtaining 3.5 $mmol_{NH3}$ $g_{cat.}^{-1}$ $h^{-1}$ [4]. However, the main challenge in catalysis lies on the preparation of more efficient and selective catalysts by active site engineering. In thermal catalysis, it is typically accepted that size reduction of active metal nanoparticles promotes an enhancement of the catalytic activity due to the exposure of a larger number of surface atoms per volume unit as well as the higher number of unsaturated coordination positions and defects [5]. Thus, metal clusters containing hundreds to few atoms, or even single metal atom catalysts are currently widely investigated as efficient and selective catalysts. Recently, Jiang group comprehensively studied the size sensitivity of supported mono/bimetallic Ru-based catalysts for ammonia production and revealed that the atomic clusters instead of single atoms or nanoparticles exhibited the highest ammonia production rate by a facilitated nitrogen activation [6,7]. The above works again highlight the importance of precisely control the catalyst size to obtain highly active ammonia production catalyst. However, a precise control

* Corresponding authors.
*E-mail addresses:* joalsan6@upvnet.upv.es (J. Albero), hgarcia@qim.upv.es (H. García).

https://doi.org/10.1016/j.apcatb.2023.123143
Received 15 May 2023; Received in revised form 11 July 2023; Accepted 31 July 2023
Available online 1 August 2023
0926-3373/© 2023 Elsevier B.V. All rights reserved.

in size distribution during the preparation of sub-nanometric active sites still remains challenging, especially at the large scale, as consequence of their tendency to undergo agglomeration and particle growth.

Metal-organic-frameworks (MOFs) have attracted much attention in the last decades as photocatalysts for that it presents several advantages over other alternative materials such as very large specific surface area, flexible design, micro- or mesoporous structures, and the possibility to incorporate a large variety of organic moieties or metals [8]. Moreover, MOFs have recently demonstrated that can act as templates or precursors of very different materials including metal single atoms and clusters [9,10]. The use of MOFs as sacrificial templates offers the advantage that the structure and chemical properties of the initial MOFs generally determine the morphology and porosity of the resulting materials. In fact, the use of MOFs as templates or precursors provide materials that exhibit excellent performance in different applications such as supercapacitors, [11] electrocatalysis, [12] photocatalysis [13] and thermal catalysis [14]. For instance, Zhang et al. have recently reported photocatalytic $H_2$ production with 56 % quantum efficiency using Cu single atoms anchored on $TiO_2$ [15]. The high loading of highly dispersed Cu single atoms was achieved by anchoring Cu ions on MIL-125 MOF, and subsequent calcination, forming a metal-oxygen-titanium bond, which was found key to ensure uniformly immobilized metal single atoms while enabling at the same time high density of these single atom sites.

Herein, we report the preparation of Cs-decorated small Ru clusters (< 1 nm) homogeneously dispersed on $ZrO_2$ using UiO-66 MOF as template. The as-prepared material presents highly dispersed sub-nanometric Ru clusters at 2.5 wt % loading. The optimized photocatalyst has demonstrated a $NH_3$ production rate at atmospheric pressure and 350 °C in dark of ~1.6 mmol·$g_{cat}^{-1}$·$h^{-1}$ (64 $mmol_{NH3}$ $g_{Ru}^{-1}$ $h^{-1}$), while the activity increases by over 300 % upon 1 Sun intensity light (1080 W $m^{-2}$) irradiation, reaching 5.1 mmol $g_{cat}^{-1}$ $h^{-1}$ (204 $mmol_{NH3}$ $g_{Ru}^{-1}$ $h^{-1}$). Ru clusters prepared by impregnation method on commercial $ZrO_2$ exhibited almost 1 order of magnitude lower $NH_3$ production rate, stressing the convenience of the MOF template method. Mechanistic studies have determined that non-thermal hot electron injection and photothermal mechanisms operate simultaneously, improving the overall efficiency of the photocatalytic process. Moreover, this photocatalyst has demonstrated to be stable for at least 100 h of continuous irradiation under these conditions.

## 2. Experimental section

### 2.1. Materials preparation

*Synthesis of UiO-66(Zr).* UiO-66(Zr) was synthesized according to the previous reported work. Specifically, terephthalic acid (0.33 g, 2 mmol) and $ZrCl_4$ (0.46 g, 2 mmol) were added to a Teflon-lined autoclave containing DMF (6 mL). The sealed Teflon was heated at 200 ºC for 12 h. After cooling to room temperature, the resulting white precipitate was washed with DMF at 120 ºC for 2 h (three times) under vigorous stirring and, then, the DMF was extracted by methanol in a Soxhlet system. Finally, the solid was dried in vacuum at 150 ºC for overnight.

*Synthesis of Cs(x)Ru(y)@$ZrO_2$.* In a typical procedure for the synthesis of Cs(6)Ru(2)@$ZrO_2$ (6 indicating the approximate Cs/Ru atomic ratio and 2 corresponding to the rough percentage of Ru on the material), 200 mg/mL of UiO-66(Zr) suspension was impregnated with 4.1 mg (20 μmol) of $RuCl_3$ by sonicating in water bath for 1 h, followed by adding 23 mg (120 μmol) of $CsNO_3$. Subsequently, the water was slowly evaporated at 75 °C under gentle stirring, and then, dried at 150 °C under vacuum for 3 h. Finally, the Cs/Ru incorporated UiO-66 was subjected to calcination at 550 °C for 2 h and the obtained Cs(6)Ru(2)@$ZrO_2$ catalyst was directly used without further treatment.

The synthesized of Cs(x)Ru(y)@$ZrO_2$ with different Cs and Ru loading was prepared following the same protocol as that for Cs(6)Ru(2)@$ZrO_2$.

### 2.2. Photocatalytic tests

Photo-assisted nitrogen fixation tests were performed in a customized fixed-bed photothermal reaction system as reported previously by our group [4]. In a typical experiment, the photocatalyst (50 mg) was loaded on the fused quartz frit placed inside a borosilicate glass tube reactor. External heating was supplied by an electrical heating mantle wrapped on the walls of the flow reactor and the temperature at the photocatalyst bed was monitored by a K-type thermocouple connected to the electrical heater controller. A 300 W xenon lamp (1080 W/$m^2$) was used to irradiate the surface of the photocatalyst through a quartz tube that was mounted on the top of the reactor. The spot of the light source on the catalyst surface was 10 mm in diameter, ensuring a collimated beam that irradiates uniformly the whole catalyst surface. The heat due to light irradiation on the catalyst surface has been measured. Consequently, the external heating has been corrected accordingly, and the indicated temperatures are the result of the combined external electrical heating and the heat due to light irradiation. Before each test, the catalyst was activated with $H_2$ for 2 h at 350 °C and the effluent of the last 30 min of the activation process was collected and analyzed to exclude any possible $NH_3$ contamination from the system or the photocatalyst. The feeding gases ($H_2$ 45 mL/min and $N_2$ 15 mL/min) were purified by passing them through 5 mM $H_2SO_4$ acid, milli-Q water and $CaCl_2$ dryer in sequence before introducing them into the reactor. The produced $NH_3$ was trapped by 5 mM $H_2SO_4$ acid and then quantified by indophenol blue method and $^1H$ NMR spectroscopy. For the determination of the reaction order, variable $H_2$ or $N_2$ flow rate, compensated by argon flow to have a constant total flow of 60 mL/min, was introduced into the system under dark or upon light irradiation conditions. Specifically, four groups of feeding gas of ($H_2$, $N_2$, Ar) with different flow rates (mL/min) of (5, 15, 40), (10, 15, 35), (15, 15, 30) and (25, 15, 20) were employed in the determination of the $H_2$ partial reaction order. Four other groups of feeding gas of ($N_2$, $H_2$, Ar) with different flow rates (mL/min) of (5, 15, 40), (10, 15, 35), (15, 15, 30) and (25, 15, 20) were used for determination of the $N_2$ partial reaction order. The $NH_3$ production rates were calculated based on the mass of loaded catalyst, unless otherwise noted (for example, $mmol_{NH3}$ $g_{Ru}^{-1}$ $h^{-1}$ is the rate based on the mass of Ru).

### 2.3. $^{15}N_2$ isotopic experiment

$^{15}N_2$ isotopic experiment was performed in a photo-assisted nitrogen fixation set-up as described above modified by recirculating the exit gases in a recirculation system. Specifically, a rubber suction bulb, together with a "T" connector were used to collect the inlet and outlet of the flow reaction set-up. In a typical test, the feeding gas of $H_2$ and $^{15}N_2$ was filled in sequence to the close circulation system after it was thoroughly purged with argon gas. Afterwards, the mixture gas was manually circulated by means of the rubber suction bulb inside the system for 30 min under the typical reaction conditions. The $^{15}NH_3$ collected at the 5 mM $H_2SO_4$ solution was analyzed by $^1H$ NMR spectroscopy.

### 2.4. Computational details

Full geometry optimizations were carried out with Gaussian 16 package [16] using the Minnesota 2006 local functional (M06-L) [17] and def2-TZVP basis set [18] with effective core potential for Ru and Cs atoms. In addition, density fitting approximation was automatically generated and used. The stability and spin multiplicity of $Ru_6$ clusters has been studied in previous theoretical works that found that $2S + 1 = 9$ was the most stable spin state [19,20]. At M06-L/def2-TZVP level, our results suggest that the octahedral geometry ($2S + 1 = 9$) is slightly more stable than the trigonal prism. Therefore, subsequent calculations were exclusively carried out using this geometry as starting point. In order to characterize the nature of optimized structures, analyses of frequencies were also conducted showing that all optimized structures are minima

(absence of imaginary frequencies). The possibility of different adsorption points was taken into account for both $Ru_6$ and $Ru_6CsOH$ species. Molecular electrostatic potential (MEP) surfaces were computed at the same level using the 0.001 a.u. isosurface.

## 3. Results and discussion

### 3.1. Photocatalyst synthesis and characterization

Cs(6)Ru(2)@$ZrO_2$ photocatalyst was obtained by calcination at 550 °C under air atmosphere of UiO-66 MOF to which previously appropriate amounts of $RuCl_3$ and $CsNO_3$ salts were consecutively adsorbed, as depicted in Scheme 1. Experimental Section describes in detail the procedure including the amounts of the corresponding precursors and preparation protocol. After incorporation of Ru and Cs, UiO-6(Zr) MOF preserved its structure and crystallinity, as confirmed by powder X-ray diffraction (PXRD, Fig. S1 in Supporting Information) and high-resolution field emission scanning electron microscopy (HR-FESEM, Fig. S2 in Supporting Information). Calcination at the open-air results in the decomposition of UiO-66(Zr) to high crystalline $ZrO_2$ with an average particle size of 15 nm as determined by statistical analysis of the high-resolution transmission electron microscopy images (HR-TEM, Fig. 1). Two different fringe edge distances of 1.86 Å and 3.0 Å, corresponding to (112) and (101) planes of $ZrO_2$ (JCPDS. 50-1089, tetragonal) were measured. In contrast, no obvious $RuO_2$ NPs or Cs species could be discerned from HR-TEM images. The presence and amount of Ru and Cs could be, however, quantified by X-ray fluorescence that confirmed the proportion of Ru and Cs to be 2.5 wt % and 11 wt %, respectively. PXRD patterns of Cs(6)Ru(2)@$ZrO_2$ exhibited broad peaks attributable to $ZrO_2$ NPs (JCPDS. 50–1089, tetragonal), together with weak peaks that correspond to CsCl (JCPDS. 05–0607), which we propose to be formed *via* ion metathesis between $CsNO_3$ and $RuCl_3$ during calcination. No obvious peaks that could correspond to any Ru species (particularly no $RuO_2$ or metallic Ru) could be observed (see Fig. S3 in supporting Information), demonstrating the high dispersion of this element on the $ZrO_2$ support. According to previous report, the free hydroxyl group on the $Zr_6$ node can act as the coordination site for exotic cations (as shown in Scheme 1),[21] which ensured a homogeneous distribution of $Ru^{3+}$ throughout the MOF template, and consequently less chance aggregation during the calcination step.

Aberration-corrected high-angle-annular-dark-field scanning transmission electron microscopy (AC-HAADF STEM) was employed to further study the Cs and Ru distribution in Cs(6)Ru(2)@$ZrO_2$ catalyst. Due to a similar Z value of Zr (Z = 40) and Ru (Z = 44), it is challenging to distinguish Ru species from $ZrO_2$ background. However, as can be observed in Fig. 1c and d, bright dots (less than 1 nm) can be discerned from the $ZrO_2$ background. Some of these bright spots were marked in these Figures with white arrows for better identification. It is speculated that these bright dots correspond to Cs-surrounded Ru species. EDX mapping of these bright spots revealed that they contain Ru and Cs. These two elements are homogenously distributed in the whole $ZrO_2$ sample, further confirming the high Ru and Cs dispersion in Cs(6)Ru(2)@$ZrO_2$ photocatalyst. Therefore, also no actual particle dimension could be made due to the resolution of the HR-TEM instrument, it seems that 1 nm is the upper limit for Ru clusters. Otherwise it is likely that these Ru nanoparticles could have been visualized.

### 3.2. Photo-assisted nitrogen fixation tests

The activity of Cs(6)Ru(2)@$ZrO_2$ to promote photo-assisted nitrogen fixation was evaluated with a customized fixed-bed flow reactor made of quartz that allows the irradiation of the surface of the catalyst by a xenon lamp (see Experimental Section and ref [4] for a detailed information). As we have reported in our previous work, the increase of the temperature due to light irradiation was evaluated before the reaction. A maximum 12 °C with 1 sun light irradiation was observed at the external heating control setting at 350 °C (Fig. S4) [4]. Accordingly, the external heating was corrected to have a constant catalyst surface temperature [4]. As shown in Fig. 2a, the $NH_3$ production rate at 350 °C in the dark was about ~1.6 mmol $g_{cat}^{-1}$ $h^{-1}$, and the activity increased by over 300 % upon 1 Sun intensity light (1080 W/$m^2$) irradiation, reaching 5.1 mmol $g_{cat}^{-1}$ $h^{-1}$ based on the mass of Cs(6)Ru(2)@$ZrO_2$ catalyst, or 204 $mmol_{NH3}\cdot g_{Ru}^{-1}\cdot h^{-1}$ (with TOF 20.61 $h^{-1}$) based on the mass of Ru, which, to the best of our knowledge, is the highest activity reported so far under similar reaction temperature and pressure (see Table S1 in Supporting Information for a list of precedents regarding the state-of-the-art $NH_3$ production rates at atmospheric pressure). Besides the absolute value of $NH_3$ production, the three times light enhancement at only 1 Sun irradiation power is a record in the field of photothermal $N_2$ fixation, showing a high potential for practical application of this catalyst. Control experiments using UiO-derived $ZrO_2$ or a Ru clusters deposited on $ZrO_2$ (Ru@$ZrO_2$) at the same loading as Cs(6)Ru(2)@$ZrO_2$ result in negligible $NH_3$ production (Fig. S5), indicating that the activity of Cs(6)Ru(2)@$ZrO_2$ originates from the synergistic effects of all three components. Possible nitrogen species contamination from the catalyst or the reactor that could result in $NH_3$ production was excluded by the control experiment with only $H_2$ gas feed, which resulted in a negligible 0.4 μmol $g_{cat}^{-1}$ $h^{-1}$ $NH_3$ production (Fig. S5 condition A). In addition, the $^{15}N_2$ isotopic experiment showing in solution $^1H$ NMR spectroscopy the change of the N-H coupling from $^{14}N$ (triplet) to $^{15}N$ (doublet) firmly confirmed that $NH_3$ derives exclusively from $N_2$ gas as substrate (Fig. S6).

Temperature dependence of the $NH_3$ production rate was studied in the range from 200 to 350 °C, either in the dark or upon 1 Sun intensity xenon lamp irradiation. As shown in Fig. 2a, the reaction rates increase exponentially along with the reaction temperature in both light irradiation and in the dark, suggesting that light enhancement occurs by promoting a photothermal mechanism analogous to a thermal process. The light enhancement is presented in the inset in Fig. 2a, in which a sigmoidal curve decreasing from 40 to 4 times enhancement was observed along with the temperature. The higher light enhancement at relatively lower temperature indicates that apart from the photothermal

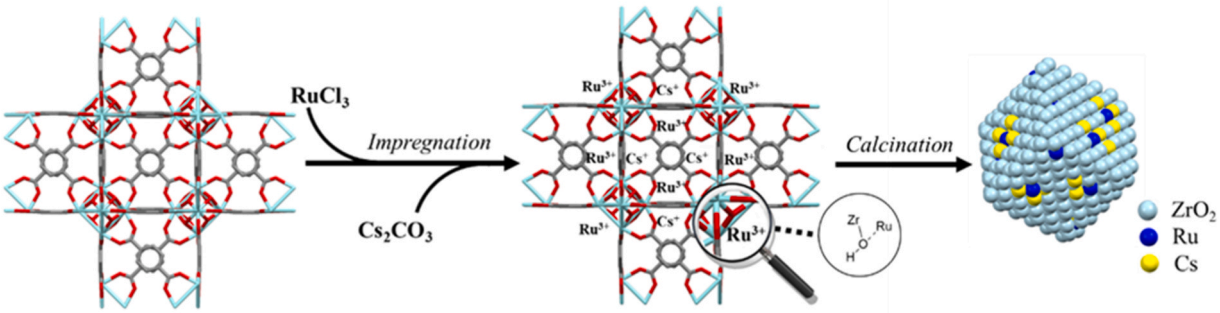


**Scheme 1.** Main steps in the Cs(6)Ru(2)@$ZrO_2$ photocatalyst preparation.

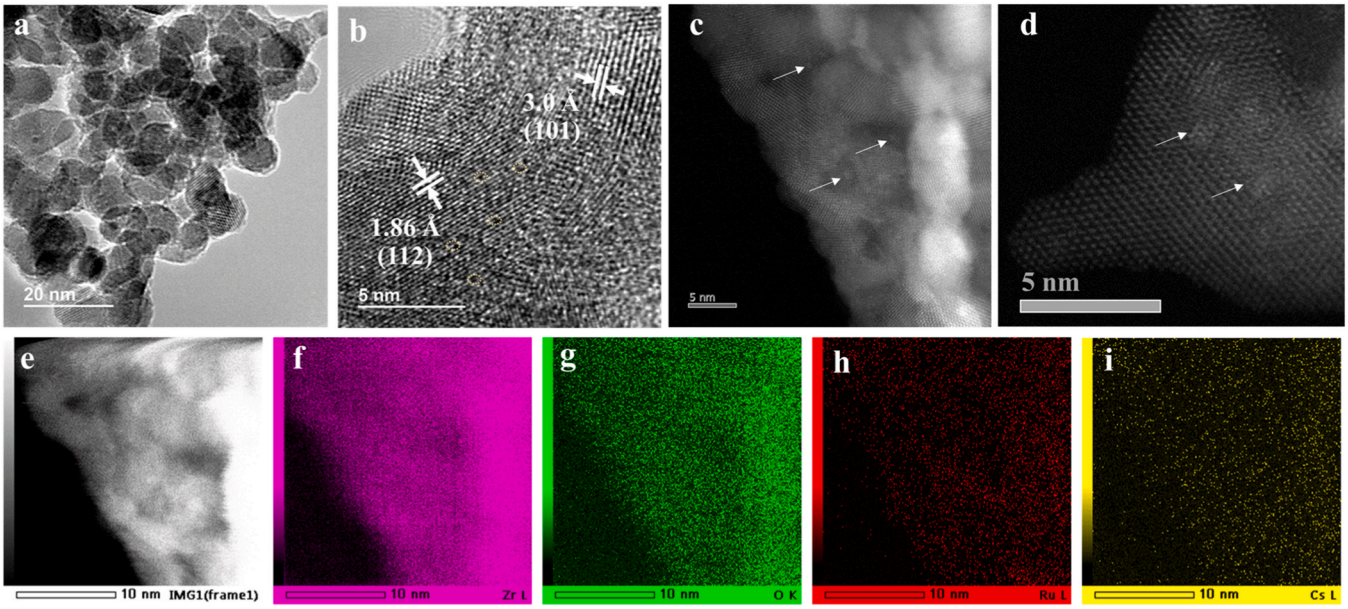


**Fig. 1.** (a) and (b) HR-TEM images, (c) and (d) aberration corrected HAADF STEM images (the white arrows point to $Cs^{+}$-surrounded Ru clusters), (e)-(i) EDX elemental mapping acquired from Cs(6)Ru(2)@$ZrO_2$ catalysts: f) Zr, g) O, h) Ru and i) Cs.

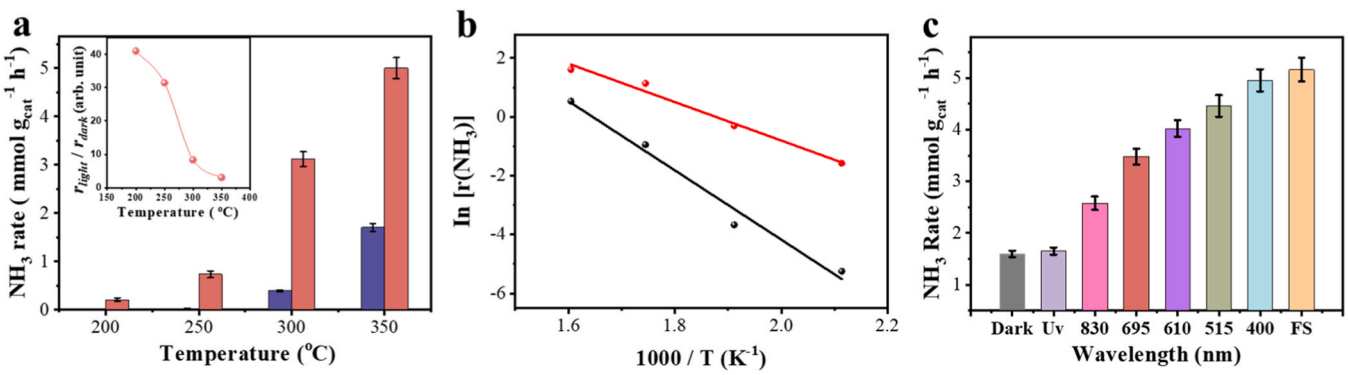


**Fig. 2.** (a) Temperature dependence of $NH_3$ production rate with using Cs(6)Ru(2)@$ZrO_2$ as catalyst under dark (blue columns) and light irradiation (red columns). The inset shows the light enhancement. (b) Arrhenius plot under dark (black dots and best linear fitting) and light irradiation (red dots and line). (c) NH3 production rate under dark conditions and upon light irradiation using different cut-off filters (FS: full Xe lamp spectrum, the number indicates the filter nominal shorter wavelength). Reaction conditions: catalyst 50 mg, feeding gas 15 mL $min^{-1}$ $N_2$ + 45 mL·$min^{-1}$ $H_2$, atmospheric pressure, temperature 350 °C, light source 1080 W $m^{-2}$ (300 W Xe lamp). The error bars correspond to the standard deviation of three independent measurements, and the centre value for the error bars is the average of the three independent measurements.

effects, a photocatalytic pathway of $N_2$ activation and reduction also plays an important role at low reaction temperatures. Arrhenius plots for both light and dark conditions are shown in Fig. 2b, in which a linear relationship is observed in the range of temperatures from 200 to 350 °C for both light and dark conditions, with slope values of − 6.76 and − 11.03, respectively. It has been widely accepted that the interaction of nanoparticles and the incident light can result in high localized temperature, which cannot be precisely determined by conventional thermometers. The macroscopic temperature measured by contacting the thermocouple on the catalyst surface is usually employed for estimating the activation energy of the Arrhenius plot [22]. Hence, in the present case, the activation energies were estimated to be 56 and 91.7 kJ $mol^{-1}$ for light irradiation and the dark reaction, respectively. The relatively lower activation energy upon light irradiation indicates again that the light must facilitate the $N_2$ reduction process through a different mechanism than the purely photothermal one (coincident activation energy for both processes), probably involving photocatalytic $N_2$ electron reduction (*vide infra*).

In order to stress the advantages of the herein employed MOF templated method for the Ru(6)Cs(2)@$ZrO_2$ preparation, a photocatalyst containing the same Ru and Cs loadings supported on commercial $ZrO_2$ (Ru(6)Cs(2)@$ZrO_2$-S) was also synthesized *via* a conventional impregnation method. HR-TEM images (Fig. S7) revealed the presence of Ru NPs over 10 nm loaded on the surface of $ZrO_2$, demonstrating the essential role of the MOF-templated method in order to obtain highly dispersed small Ru clusters. Furthermore, the BET surface area of Ru(6)Cs(2)@$ZrO_2$ and Ru(6)Cs(2)@$ZrO_2$-S are 1.767 $m^2$/g and 42.66 $m^2$/g, respectively (Fig. S8). The over 20 times larger of surface area can contribute to higher accessible active sites in Ru(6)Cs(2)@$ZrO_2$, which should also increase the activity for $NH_3$ production. The photoassisted ammonia production rate using Ru(6)Cs(2)@$ZrO_2$-S was only 0.73 mmol $g_{cat}^{-1}$ $h^{-1}$, which is almost 7 times lower than that of Ru(6)Cs(2)@$ZrO_2$, highlighting the convenience of the synthetic strategy starting from UiO-66 MOF.

### 3.3. Photo-assisted mechanism

The influence of incident light wavelength range on the photo-

assisted $NH_3$ production rate was studied to gain further insights into the underlying mechanism of the photo-assisted $N_2$ hydrogenation. Specifically, full spectrum without optical filter (noted as **FS** in the x axis in Fig. 2c), visible cut filters (cutting transmission of visible radiations of wavelength > 380 nm, noted as **Uv** in the x axis in Fig. 2c) and sharp cut filters (allowing the transmission of light with wavelength > 400, 515, 610, 895 and 830 nm, respectively, noted as the corresponding number in the x axis in Fig. 2c) were applied to the reaction in sequence. As can be seen in Fig. 2c, compared to the $NH_3$ production rate under dark condition at 350 °C (1.6 mmol $g_{cat}^{-1}$ $h^{-1}$), UV light irradiation up to 380 nm results in only 0.06 mmol $g_{cat}^{-1}$ $h^{-1}$ of enhancement, which accounts for only 5.1 % of the total 300 % times light enhancement by irradiation with the full Xe spectrum. Whilst the $NH_3$ production rate reached 2.57 mmol $g_{cat}^{-1}$ $mol^{-1}$ upon the irradiation of NIR light (xenon lamp light filtered with a cut-off filter λ > 830 nm), which makes up 81 % of the light enhancement. The rest 213 % of the light-enhanced activity comes from the visible light region from 400 nm to 830 nm.

To correlate the photo-assisted activity and the light response of each component, diffuse reflectance UV-Vis-NIR spectra were recorded for both Cs(6)Ru(2)@$ZrO_2$ and $ZrO_2$ samples (Fig. S9). Bare $ZrO_2$ support exhibited a characteristic absorption band at ~370 nm, and it lacks photoresponse in the visible to NIR range, ruling out its role as 'photon antenna' or 'photosensitizer' in the photo-assisted reaction. On the contrary, the loading of Ru onto the $ZrO_2$ support results in broad absorption band spanning from 200 to 2000 nm, which should be responsible for the wavelength-dependent activity enhancement. It has been reported that metallic Ru clusters possess a very broad plasmon band extending from the visible to the NIR, and hence the visible to NIR range photoresponse can be attributed to the plasmonic effect of Ru clusters, even their small size. The contribution of the presence of a small residual percentage of C from the terephthalate linker acting as dopant of Ru cannot be disregarded. As a consequence, light absorption by Ru NP plasmon band results in highly localized temperature, [23] and eventually, an enhanced $NH_3$ production rate. In other studies, Jiang and coworkers have reported that a decrease in Ru cluster size increases its activity for $N_2$ activation [6,7].

It has been shown in Fig. 2b that the activation energy decreases upon light irradiation and this apparent lower activation barrier is compatible, to some extent, with a reaction pathway through a non-thermal way, [24] since thermal and photothermal pathways should have a coincident activation energy. However, since the activation energy was obtained based on the macroscopic temperature, this conclusion still needs to be supported on a firm ground. To confirm the non-thermal contribution, parameters that are independent of the reaction temperature, but related to the reaction mechanisms as reagent reaction order should be measured. In this case, the reaction orders of the reagents were established by varying the reactant partial pressure under otherwise constant reaction conditions and some valuable kinetic information was attained by comparing the partial reaction order in the dark and under light irradiation. Fig. 3 presents the partial reaction order for $N_2$ and $H_2$ both in the dark and upon irradiation. As can be observed there, the $N_2$ reaction order decreased from 0.89 in dark to 0.70 upon light irradiation, indicating that light facilitates the activation/reaction of $N_2$. It is proposed that the higher reactivity of $N_2$ under illumination would be due to the transfer of hot electrons generated upon excitation of Ru NP plasmon band into the anti-bonding orbitals of adsorbed $N_2$, weakening the N≡N triple bond. The decrease of the reaction order for $N_2$ also agrees with the decrease of the apparent activation energy under illumination as shown in Fig. 2b. Interestingly, the $H_2$ reaction order changed from − 0.5 in dark to + 0.47 in the presence of light irradiation. The negative reaction order in dark conditions indicates that the $H_2$ adsorption, presumably by dissociation into hydride, blocks the active sites, hindering as consequence $N_2$ activation and making the reaction slower [25,26]. Upon light irradiation, on one hand, $N_2$ activation becomes favored due to its lower activation barrier increasing hydride consumption compared to the dark, increasing, consequently, the $H_2$ reaction order. On the other hand, it has been previously reported that the light irradiation facilitates the reductive elimination of hydride from the metal center desorbing $H_2$ [27]. In the present case, we propose that the equilibrium of reversible $H_2$ adsorption-desorption was disfavored upon light irradiation. More specifically, the light irradiation results in a higher desorption rate due to the higher electron density on Ru nanoparticles due to the operation of surface plasmonic effects. Overall, a positive $H_2$ partial reaction order results from the operation of these two effects. Combining the kinetic data obtained from activation energy tests and reagent reaction order studies, it can be concluded that there are differences in the thermal and light-assisted mechanism that can be ascribed to photogenerated hot electrons assisting the reaction.

To further confirm the non-thermal-hot electron mechanism, photocurrent response of a Ru(2)@$ZrO_2$ electrodes under Ar or $N_2$ atmosphere were studied. Additionally, a control experiment using a $ZrO_2$ electrode under $N_2$ atmosphere was also carried out, and the results are presented in Fig. S10. As can be observed, Ru(2)@$ZrO_2$ electrode shows an abrupt increase in the photocurrent (from ~ −11 μA to ~18 μA) upon light irradiation (λ > 450 nm). The observed photocurrent in Ru(2)@$ZrO_2$ electrode under $N_2$ atmosphere is much higher than that in Ar atmosphere, indicating that $N_2$ is reacting with the Ru(2)@$ZrO_2$ electrode under light conditions, and demonstrating that the light irradiation on the electrode induces hot electrons and facilitate the $N_2$ reduction process. It is worth commenting that the onset absorption edge of $ZrO_2$ is ~370 nm (Fig. S9), and hence, the photocurrent can only be attributed to the hot electrons induced by the interaction of Ru clusters and the incident light. Furthermore, the negligible photocurrent

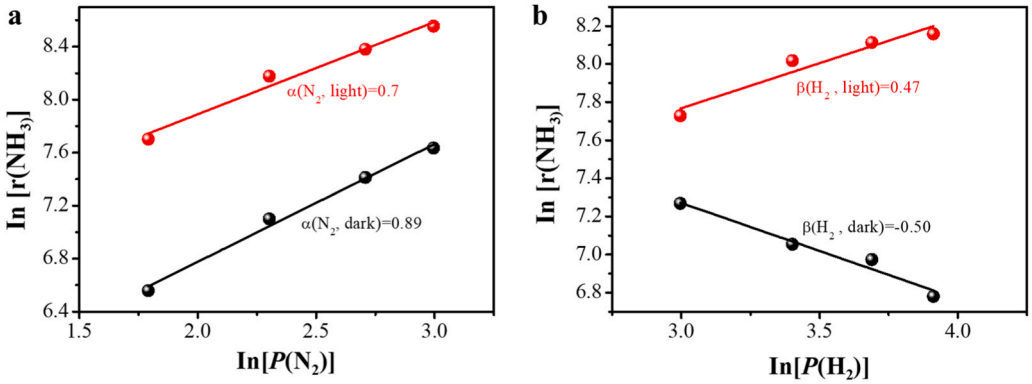


**Fig. 3.** Dependence of the $NH_3$ production rate on (a) $N_2$ partial pressure in the dark (black sphere) and under light irradiation (red sphere), and (b) dependence on the $H_2$ partial pressure in the dark (black sphere), and upon light irradiation (red sphere) with Cs(6)Ru(2)@$ZrO_2$ catalyst at 350 °C under atmospheric pressure. Light Source: xenon lamp 1080 W/$m^2$.

response in $ZrO_2$ under $N_2$ atmosphere, confirms that the hot electrons on the Ru clusters participate in the $N_2$ activation.

### 3.4. Cs promoter effects

The influence of Cs loading on the $NH_3$ production rate was also studied to clarify the role of Cs on the catalytic activity. As presented in Fig. S11, in the absence of Cs, Ru(2)@$ZrO_2$ catalyst exhibits a $NH_3$ production rate of 2.5 μmol $g_{cat}^{-1}$ $h^{-1}$ at 350 °C upon 1080 W/$m^2$ light irradiation. No remarkable activity enhancement was observed when the Cs to Ru atomic ratio increased from 0 to 3.5, with only 29.3 μmol $g_{cat}^{-1}$ $h^{-1}$ $NH_3$ production rate achieved. Surprisingly, a drastic enhancement of 170 times was achieved for a Cs to Ru ratio at 6, reaching a $NH_3$ production rate of 5.1 mmol $g_{cat}^{-1}$ $h^{-1}$. Further increasing the Cs to Ru ratio to 10 decreases the catalyst activity, dropping down to 2.98 mmol $g_{cat}^{-1}$ $h^{-1}$. Therefore, the maximum effect was observed for a Cs to Ru ratio of 6. The dependence of $NH_3$ production activity on the amount of Cs loading in dark condition also follows the same trend as that upon irradiation, with a $NH_3$ production rate of 0.0018, 0.011, and 1.6 mmol $g_{cat}^{-1}$ $h^{-1}$ for Cs to Ru ratio at 0, 3.5 and 6, respectively. Observation of the same trend in the dark and under light irradiation suggests that the role of Cs promoting the reaction is the same under both conditions. It should be reminded that chloride adsorbed on metallic sites, such as Au and Ru, leads to deactivation due to its strong binding to the metal [28,29]. Following this clue, it can be reasonably speculated that one of the roles of $CsNO_3$ is to remove chloride from Ru. This hypothesis is in accordance with the previously commented PXRD data (Fig. S3) that shows the formation of CsCl in the calcination process. In addition, the value 3.5 matches with the stoichiometry of $RuCl_3$ reacting with $CsNO_3$ since the consumption of the chloride needs at least three $CsNO_3$ molecules for each Ru.

The decomposition of $CsNO_3$ was also confirmed by XPS characterization. The N1s spectrum of Cs(6)Ru(2)@$ZrO_2$ revealed negligible amount of nitrogen species in the sample (Fig. S12a), demonstrating the decomposition of nitrate during the calcination step. In addition, it can be observed from Fig. 4a that Cs(6)Ru(2)@$ZrO_2$ before activation contains a high proportion of the component attributable to carbonate (~289 eV), which would be derived from the reaction of cesium hydroxide/oxide with ambient $CO_2$ since these Cs species are strongly basic (Eq. (1)). In contrast, the Ru(2)@$ZrO_2$ sample in the absence of Cs exhibited very low concentration of carbonate (Fig. 4b), ruling out the possibility that carbonate correlates with the $ZrO_2$ support. It must be noted that, even though evidenced by XPS, the formation of $Cs_2CO_3$ was not observed in XRD (Fig. S3). The absence of $Cs_2CO_3$ diffraction pattern in Cs(6)Ru(2)@$ZrO_2$ sample should be attributed to the high dispersion of $Cs_2CO_3$ on $ZrO_2$, as it has been reported that the Cs species prone to localize in the vicinity of Ru active center [30]. Besides the evidence of $CsNO_3$ decomposition, the XPS spectrum of Cs(6)Ru(2)@$ZrO_2$ (Fig. 4a) also revealed the formation of $RuO_2$ after the calcination, as evidenced by peaks centered at 286.1 and 281.9 eV, which correspond to the $Ru^{4+}$ $3d_{3/2}$ and $Ru^{4+}$ $3d_{5/2}$, respectively. The component peaking at 284.9 eV can be attributed to $sp^2$ carbon.

$$2CsOH + CO_2 \rightarrow Cs_2CO_3 + H_2O \quad (1)$$

At least two different Cs species in Cs(6)Ru(2)@$ZrO_2$ catalysts, namely, CsCl and $Cs_2CO_3$, were confirmed by PXRD and XPS, respectively. Even after the activation, the presence of Cl in the sample is still confirmed by XPS (Fig. S12b and c), and thus, it is interesting to study in which form the Cs species facilitates $N_2$ fixation reaction. Taking the advantage that the Cs salt (CsCl, $Cs_2CO_3$, and CsOH) are highly soluble in water, Cs(6)Ru(2)@$ZrO_2$ catalyst was thoroughly washed with MilliQ water and the resulting sample was tested for $N_2$ fixation. As expected, no activity was obtained, neither in dark nor upon light irradiation (see Fig. S13). Afterwards, CsCl was added to the catalyst by impregnation method, but still no activity was observed. Surprisingly, the catalytic activity was regained upon addition of $CsNO_3$, with 0.37 and 2.14 mmol $g_{cat}^{-1}$ $h^{-1}$ achieved in dark and light irradiation conditions, respectively. The amount of $NH_3$ produced during the activation process was equal to the mole amount of $CsNO_3$, indicating all the $NO_3^-$ has been decomposed to CsOH or $Cs_2O$ before the test (Eqs. (2) and (3)), which

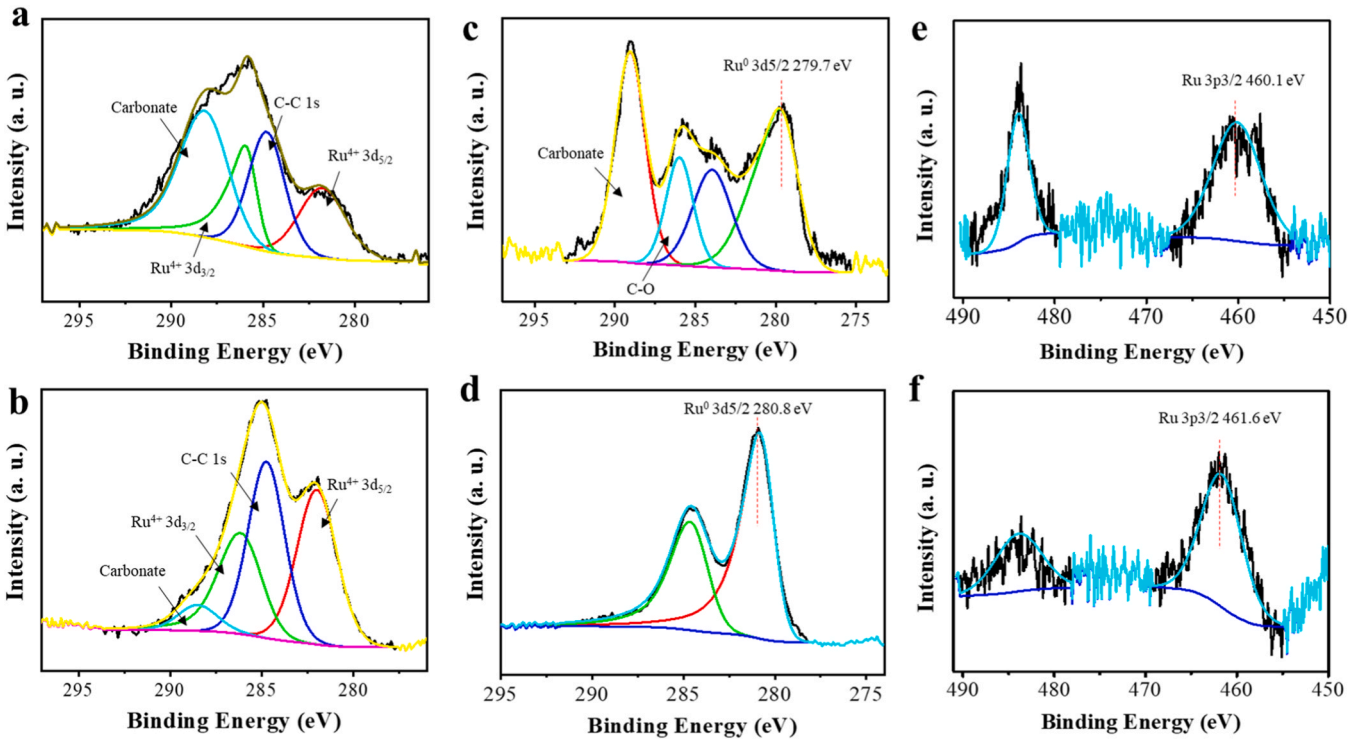


**Fig. 4.** XP spectra of Ru 3d + C1s collected from Cs(6)Ru(2)@$ZrO_2$ sample (a) before and (c) after $H_2$ activation; Ru 3d + C1s collected from Ru(2)@$ZrO_2$ sample (b) before and (d) after $H_2$ activation; Ru 3p collected from (e) Cs(6)Ru(2)@$ZrO_2$ and (f) Ru(2)@$ZrO_2$ after $H_2$ activation.

are generally regarded as the real species that facilitate the $N_2$ activation. In addition, the absence of $CO_2$ in the activation process excludes the possible formation of $Cs_2CO_3$ as the active Cs species. However, impregnation of $Cs_2CO_3$ as the initial Cs precursor instead of $CsNO_3$ also results in identical activity (Fig. S13, condition 5). Presumably, $Cs_2CO_3$ can also be decomposed to CsOH or $Cs_2O$ species during the activation process.

$$2CsNO_3 + H_2 \xrightarrow{350^oC} 2CsOH + 2NO_2 \quad (2)$$

$$2CsNO_3 + H_2 \xrightarrow{350^oC} Cs_2O + 2NO_2 + H_2O \quad (3)$$

Upon *in-situ* activation at 350 °C for 2 h, the Ru $3d_{5/2}$ peak of Ru(2)@$ZrO_2$ shifts from 282 eV to 280.8 eV, indicating the reduction of $RuO_2$ to metallic Ru species (Fig. 4b and d). The Cs(6)Ru(2)@$ZrO_2$ after the activation shows even lower Ru binding energy, with Ru $3d_{5/2}$ component peaking at 279.7 eV, together with COO and C-O components at 289 and 286 eV (Fig. 4c). The negative shift of $Ru^0$ binding energy in the presence of Cs indicates the back-electron donation from Cs species to Ru clusters, and as a consequence, an increased electron density on the Ru clusters, which finally facilitates the $N_2$ activation and its hydrogenation [4]. The negative shift of the Ru binding energy was also observed in Ru 3p spectrum, in which a 1.5 eV shift to lower binding energy from 461.6 to 460.1 eV was observed (Fig. 4f and e). Furthermore, a higher binding energy of Cs $3d_{5/2}$ (724.8 eV, Fig. S14) compared to the reported $Cs^+$ (724.0 eV), but still lower than that of metallic Cs (726.0 eV), indicates the $Cs^+$ was partially reduced with an average oxidation state $0 < \delta < 1$. Tending to be $Cs^+$, $Cs^{\delta+}$ can donate electron density to the adjacent $Ru^0$ [4,30,31]. In addition, it can be observed in Fig. S14 that O1s peak for both Ru(2)@$ZrO_2$ and Cs(6)Ru(2)@$ZrO_2$ samples exhibit a main peak at 530 eV corresponding to $ZrO_2$. However, in the case of Cs(6)Ru(2)@$ZrO_2$, a higher contribution of $OH^-$ (531.4 eV) population to the O1s peak is observed, indicating that the $Cs_2CO_3$ partially decomposed to CsOH during the activation process. The presence of basic sites due to Cs oxide/hydroxide species in close contact with the Ru surface could favor the split hydrogen atoms on Ru surface into proton−electron pairs by abstracting the $H^+$ onto the basic sites, while the electrons remain onto the Ru cluster, increasing consequently the electron density on Ru cluster [32]. In addition, these additional $OH^-$ would result in higher basicity, favouring $N_2$ adsorption and subsequent activation [4].

To further study the influence of Cs species on the electron density and acidity of active sites in Cs(6)Ru(2)@$ZrO_2$, CO chemisorption on both Ru(2)@$ZrO_2$ and Cs(6)Ru(2)@$ZrO_2$ was performed by monitoring the process by Fourier-Transformed Infrared Spectroscopy (FT-IR). Before collecting the spectra, the samples were activated at 350 °C *in-situ* under $H_2$ atmosphere to simulate the reaction conditions. Fig. S15a shows the evolution of IR spectra of Ru(2)@$ZrO_2$ in the CO vibration region (2300–1900 $cm^{-1}$) upon increasing CO pressure. As can be observed, a broad band peaking at ~2050 $cm^{-1}$ appears initially at low CO pressure, accompanied by a component at ~2189 $cm^{-1}$. The peak at 2050 $cm^{-1}$ is attributed to CO adsorbed linearly on metallic Ru, [33] whilst the band at ~2189 $cm^{-1}$ can be attributed to the CO weakly adsorbed on $Zr^{4+}$ surface sites. Upon increasing the CO pressure, the peak of CO adsorbed on weaker acid $Zr^{4+}$ site increases, and new peaks centered at 2153 $cm^{-1}$ emerged, which can be assigned to CO aggregates on $Ru^0$ sites [33,34]. Cs(6)Ru(2)@$ZrO_2$ sample exhibited also the broad band attributable to CO adsorbed on Ru sites, but with 37 $cm^{-1}$ redshift to 2013 $cm^{-1}$, providing an additional experimental support for the higher electron density on Ru sites when Cs is present in comparison to that of Ru(2)@$ZrO_2$ (Fig. S15b). It must be noticed that the intensity of this peak is much lower than that of Ru(2)@$ZrO_2$, suggesting the decrease of exposed Ru atoms due to the partial coverage by Cs species. Upon increasing the CO pressure, another band attributed to multiple CO adsorption on each Ru sites appeared at ~2137 $cm^{-1}$, the wavenumber being also redshifted in comparison to that of Ru(2)@$ZrO_2$, further confirming a higher electron density on Ru sites due to the presence of Cs. The absence of CO absorption signal from $Zr^{4+}$ sites could be attributed to the neutralization of the surface acidity by the CsOH species derived from the $CsNO_3$ decomposition [35]. The effect of Cs neutralizing acidic $Zr^{4+}$ ions was also confirmed by isothermal $CO_2$ adsorption measurement, which revealed 2-fold of $CO_2$ uptake capacity after the incorporation of Cs species (Fig. S16). Based on the CO-FTIR spectroscopic results, it can be concluded that the higher electron density of Ru sites, and a more basic support favor the activation of adsorbed $N_2$, resulting in an enhanced $NH_3$ production rate.

Density Functional Theory (DFT) calculations at M06-L/def2-TZVP level of theory were carried out to understand the static adsorption states of Ru sub-nanoclusters ($Ru_6$). Although the real Ru clusters will have probably a larger number of Ru atoms, the selection of $Ru_6$ represents a good compromise between the real Ru sites and computational cost. The electrostatic potential on Ru atoms is always positive ($V_s \approx$ 22 kcal/mol) (Fig. 5); therefore, it is expected that they behave as adsorption sites. On the other hand, the effect of a partially covered surface by Cs atoms was also considered introducing one Cs atom in our models. This introduction has a significant influence on electrostatic potential $V_s$ values above the Ru center. In quantitative terms, an important decrease of $V_s$ values was obtained for those Ru atoms located at the surroundings of Cs, while the most distant Ru atom almost remained unchanged ($V_s \approx$ 16 kcal/mol). This calculation agrees with the observed electron donation effect of Cs on Ru previously commented.

Our DFT calculations yield a feasible adsorption of molecular $N_2$ on the top of any Ru atom with an adsorption free energy $\Delta G_{ads}$ of − 0.85 eV ($r_{N\cdots Ru} \approx$ 2.0 Å). In addition, this adsorption is characterized by a slightly lengthening of N-N bond length of 0.03 Å from the computed internuclear equilibrium distance ($r_{eq}$ = 1.095 Å) which suggests an initial weak pre-activation of $N_2$. On the other hand, the introduction of a Cs atom in the cluster ($Ru_6$CsOH) strongly modifies the adsorption of $N_2$ in agreement with computed MEP values. Two possibilities were explored (Fig. 5b, **I** and **II**). In particular, the adsorption at the Cs-Ru interface proved to be the strongest adsorption site ($\Delta G_{ads} \approx$ −1.09 eV, state **II**). In this situation, a simultaneous adsorption takes place involving both Cs and Ru species, therefore, explaining the role of Cs in the catalyst near Ru clusters. In addition, the stronger adsorption correlates with a longer N-N bond length of 1.15 Å, larger than the obtained for the $Ru_6$ cluster, indicating a certain $N_2$ preactivation. The other adsorption state (**I**) involves a distant Ru atom (Cs as reference) and it is associated with a $\Delta G_{ads}$ of − 0.79 eV. The geometrical features indicate that this state is similar to the $Ru_6$ cluster, with no much influence of the Cs presence in the cluster. Thus, spatial proximity appears to be a prerequisite for a stronger $N_2$ activation.

### 3.5. Reaction mechanism

*In-situ* FT-IR spectroscopy was employed to study the reaction mechanism as reported before [4]. First, Cs(6)Ru(2)@$ZrO_2$ was *in-situ* reduced in the FT-IR chamber at 350 °C under $H_2$ atmosphere for 2 h. Then, $H_2$ and $N_2$ gases were sequentially introduced into the chamber in opposite sequences, in order to confirm if the firstly introduced feeding gas ($H_2$ or $N_2$) could form detectable adsorbed activated species, and, if $NH_3$ is finally produced when the two reagents ($N_2$ or $H_2$) are sequentially fed to the system. It must also be commented that before the gas change, the FT-IR chamber was purged with Ar for 15 min to remove the free gaseous molecules introduced in the previous step. This ensures that the two gases are not simultaneous in the FT-IR chamber. As shown in Fig. 6a, no $NH_3$ signal was detected by firstly introducing $H_2$ and subsequently $N_2$. Whilst the typical peaks attributed to $NH_3$ molecules were detected in the gas phase by first introducing $N_2$, and then the $H_2$ gas. These results indicate that activated $N_2$ species, adsorbed on the active sites, are subsequently hydrogenated, forming, thus, $NH_3$ as the final product.

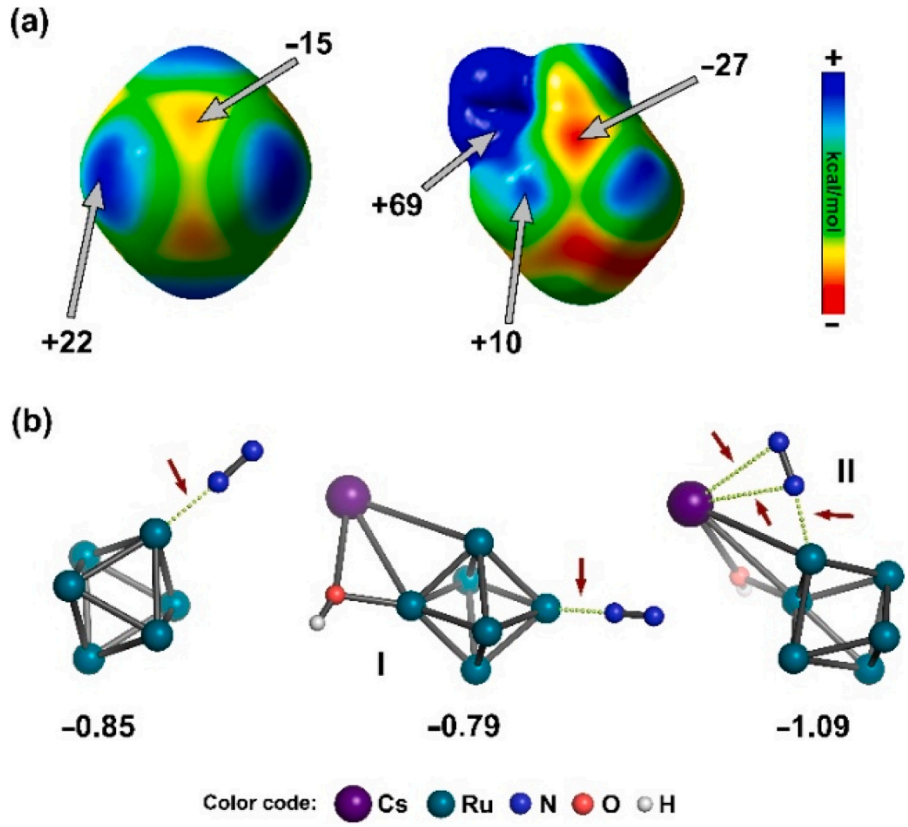


**Fig. 5.** (a) Molecular electrostatic potential (MEP) plotted onto the 0.001 a.u. surface for $Ru_6$ and $Ru_6CsOH$ clusters; $V_s$ values are given in kcal $mol^{-1}$. (b) Adsorption states of molecular $N_2$ for $Ru_6$ and $Ru_6CsOH$ (states I and II) clusters optimized at M06-L/def2-TZVP level. $\Delta G_{ads}$ are given in eV.

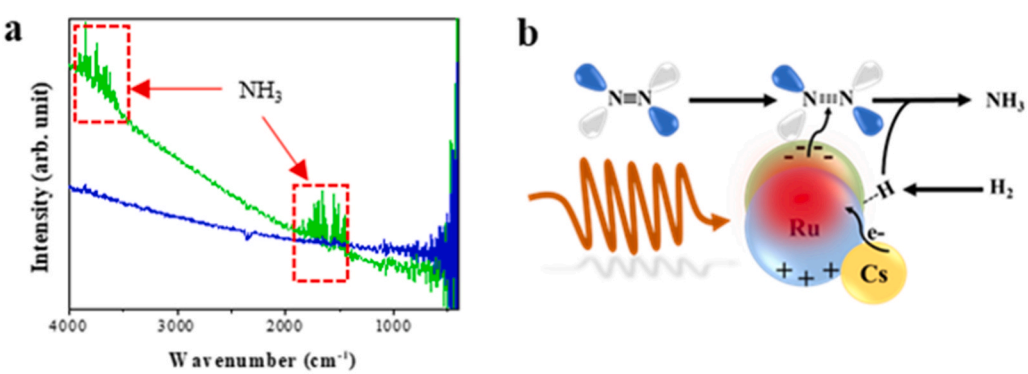


**Fig. 6.** (a) *In-situ* FT-IR spectra in gas phase after the introduction in sequence of $N_2$ and $H_2$ gas (green line) and the inverse sequence (blue line), collected at 350 °C. The chamber was purged with Ar before any gas change to remove any molecule remaining in the gas phase from the previous step avoiding the simultaneous presence in the gas phase of $N_2$ and $H_2$. (b) Pictorial illustration of the proposed mechanism of photothermal $N_2$ activation and hydrogenation to $NH_3$ by Cs(6)Ru(2)@$ZrO_2$ photocatalyst.

Based on the above studies, a reaction mechanism has been proposed regarding the photo-assisted $N_2$ fixation by Cs(6)Ru(2)@$ZrO_2$ photocatalyst, as can been seen in Fig. 6b. Metallic Ru species absorbs visible and NIR light, undergoing high localized temperature increase, due to the local surface plasmonic resonance effects (LSPR) and conversion of the photon energy into heat. Simultaneously, the LSPR also induces hot electrons that can be injected to the anti-bonding orbitals of the adsorbed $N_2$. Favored by the hot electrons injection, together with the high localized temperature at the Ru NP and the back electron donating from the CsOH species, the adsorbed $N_2$ molecules become activated and hydrogenated to form $NH_3$ with a considerable high reaction rate.

### 3.6. Photocatalysts stability

The stability of Cs(6)Ru(2)@$ZrO_2$ catalyst was evaluated by operating the photothermal reaction continuously for 100 h at 350 °C under 1080 W/$m^2$ light irradiation, measuring the $NH_3$ production rate along time. As shown in Fig. S17, the Cs(6)Ru(2)@$ZrO_2$ exhibited superior stability without activity loss during the 100 h test. Also, no changes were observed in the PXRD pattern of the 100 h-used catalyst compared to that acquired from the fresh catalyst (Fig. S18), indicating no structural changes or obvious Ru NP aggregation. It is also worth noticing that no $Cs_2O$ or CsOH species could be observed in the XRD pattern, even though those species were supposed to be the activated species of Cs promoter. The explanation for the absence is that those species are very reactive, and once exposed to ambient $CO_2$, they evolve spontaneously to $Cs_2CO_3$, as can evidenced by XPS results (Fig. 4a). In addition, the absence of $Cs_2CO_3$ diffraction pattern should be due to the high dispersion of $Cs_2CO_3$ on $ZrO_2$ support. In addition, no Ru NPs were observed in the used photocatalyst, as confirmed by HR-TEM characterization (Fig. S19).

## 4. Conclusions

This study reports the preparation of highly dispersed Cs-decorated Ru sub-nanometric clusters on $ZrO_2$ by means of UiO-66 MOF templated method. The obtained material presents an outstanding visible and NIR light response for $N_2$ fixation to $NH_3$, increasing the $NH_3$ production rate *ca.* 300 % under 1 Sun light irradiation at 350 °C and atmospheric pressure. The role of the Cs species decorating the Ru clusters has been determined to neutralize the surface $Zr^{4+}$ acidity, increasing the basicity of the $ZrO_2$ support. Moreover, the partially reduced $Cs^{\delta+}$ ($0 < \delta < 1$) species have been found to cover in part the Ru active sites, donating electron density to adjacent Ru atoms. Thus, the presence of Cs promotes the stronger adsorption of $N_2$ onto the Ru atoms, resulting in a pre-activation of the adsorbed $N_2$, as predicted by DFT calculations on models. Mechanistic studies have confirmed the co-existence of photothermal and nonthermal-hot electron mechanisms, improving the overall efficiency of this photocatalyst. Moreover, this photocatalysts have demonstrated an extended stability under the present reaction conditions. These results pave the way to design efficient and stable materials for photo-assisted commodity and fuels production under mild conditions.

## CRediT authorship contribution statement

Yong Peng prepared Ru and Cs on $ZrO_2$ and performed the photocatalytic study. Arianna Melillo made the pristine UiO-66. Run Shi was in charge of the high resolution TEM and EXAFs. Amparo Forneli performed additional photocatalytic measurements during manuscript revision. Antonio Franconetti carried out the computational calculations. Josep Albero supervised the work and write the manuscript draft and the revision. Hermenegildo García conceptualized the research and revised the final manuscript.

## Declaration of Competing Interest

The authors do not have any conflict of interest to declare.

## Data Availability

Data will be made available on request.

## Acknowledgements

Financial support by the Spanish Ministry of Science and Innovation (PDI2021–126071-OB-C21 financed support by MCIN/AEI/10.13039/501100011033 and by FEDER "Una manera de hacer Europa"), and Severo Ochoa (CEX2021–1230-S financed support by MCIN/AEI/10.13039/501100011033) is gratefully acknowledged. Generalitat Valenciana (Prometeu 2021–038 and MFA-2022–023 financed by European Union-Next Generation EU, through the Conselleria de Innovación, Universidades, Ciencia y Sociedad Digital) and European Union Horizon 2020 Research and Innovation Programme (FlowPhotoChem Grant Agreement 862453) are also gratefully acknowledged. J.A. thanks the Spanish Ministry of Science and Innovation for a Ramon y Cajal research associate contract (RYC2021–031006-I financed support by MCIN/AEI/10.13039/501100011033 and by European Union/NextGenerationEU/ PRTR).

## Appendix A. Supporting information

Supplementary data associated with this article can be found in the online version at doi:10.1016/j.apcatb.2023.123143.

## References

[1] D.G. Nocera, Solar fuels and solar chemicals industry, Acc. Chem. Res. 50 (2017) 616–619.
[2] X. Yang, D. Wang, Photocatalysis: from fundamental principles to materials and applications, ACS Appl. Energy Mater. 1 (2018) 6657–6693.
[3] D. Mateo, J.L. Cerrillo, S. Durini, J. Gascon, Fundamentals and applications of photo-thermal catalysis, Chem. Soc. Rev. 50 (2021) 2173–2210.
[4] Y. Peng, J. Albero, A. Franconetti, P. Concepción, H. García, Visible and NIR light assistance of the $N_2$ reduction to $NH_3$ catalyzed by Cs-promoted Ru nanoparticles supported on strontium titanate, ACS Catal. (2022) 4938–4946.
[5] L. Liu, A. Corma, Metal catalysts for heterogeneous catalysis: from single atoms to nanoclusters and nanoparticles, Chem. Rev. 118 (2018) 4981–5079.
[6] L. Li, Y.-F. Jiang, T. Zhang, H. Cai, Y. Zhou, B. Lin, X. Lin, Y. Zheng, L. Zheng, X. Wang, C.-Q. Xu, C.T. Au, L. Jiang, J. Li, Size sensitivity of supported Ru catalysts for ammonia synthesis: from nanoparticles to subnanometric clusters and atomic clusters, Chem 8 (2022) 749–768.
[7] Y. Zhang, J. Li, J. Cai, L. Yang, T. Zhang, J. Lin, X. Wang, C. Chen, L. Zheng, C. T. Au, B. Yang, L. Jiang, Construction of spatial effect from atomically dispersed Co anchoring on subnanometer Ru cluster for enhanced $N_2$-to-$NH_3$ conversion, ACS Catal. 11 (2021) 4430–4440.
[8] A. Dhakshinamoorthy, Z. Li, H. Garcia, Catalysis and photocatalysis by metal organic frameworks, Chem. Soc. Rev. 47 (2018) 8134–8172.
[9] L. Oar-Arteta, T. Wezendonk, X. Sun, F. Kapteijn, J. Gascon, Metal organic frameworks as precursors for the manufacture of advanced catalytic materials, Mater 1 (2017) 1709–1745.
[10] H. Huang, K. Shen, F. Chen, Y. Li, Metal–organic frameworks as a good platform for the fabrication of single-atom catalysts, ACS Catal. 10 (2020) 6579–6586.
[11] S. Sanati, R. Abazari, J. Albero, A. Morsali, H. García, Z. Liang, R. Zou, Metal–organic framework derived bimetallic materials for electrochemical energy storage, Angew. Chem. Int. Ed. 60 (2021) 11048–11067.
[12] Z. Song, L. Zhang, K. Doyle-Davis, X. Fu, J.-L. Luo, X. Sun, Recent advances in MOF-derived single atom catalysts for electrochemical applications, Adv. Energy Mater. 10 (2020) 2001561.
[13] M.Z. Hussain, Z. Yang, Z. Huang, Q. Jia, Y. Zhu, Y. Xia, Recent advances in metal–organic frameworks derived nanocomposites for photocatalytic applications in energy and environment, Adv. Sci. 8 (2021) 2100625.
[14] Q. Wang, D. Astruc, State of the art and prospects in metal–organic framework (MOF)-based and MOF-derived nanocatalysis, Chem. Rev. 120 (2020) 1438–1511.
[15] Y. Zhang, J. Zhao, H. Wang, B. Xiao, W. Zhang, X. Zhao, T. Lv, M. Thangamuthu, J. Zhang, Y. Guo, J. Ma, L. Lin, J. Tang, R. Huang, Q. Liu, Single-atom Cu anchored catalysts for photocatalytic renewable H2 production with a quantum efficiency of 56 %, Nat. Commun. 13 (2022) 58.
[16] M.J. Frisch, G.W. Trucks, H.B. Schlegel, G.E. Scuseria, M.A. Robb, J.R. Cheeseman, G. Scalmani, V. Barone, G.A. Petersson, H. Nakatsuji, X. Li, M. Caricato, A.V. Marenich, J. Bloino, B.G. Janesko, R. Gomperts, B. Mennucci, H.P. Hratchian, J.V. Ortiz, A.F. Izmaylov, J.L. Sonnenberg, Williams, F.Ding, F. Lipparini, F. Egidi, J. Goings, B. Peng, A. Petrone, T. Henderson, D. Ranasinghe, V.G. Zakrzewski, J. Gao, N. Rega, G. Zheng, W. Liang, M. Hada, M. Ehara, K. Toyota, R. Fukuda, J. Hasegawa, M. Ishida, T. Nakajima, Y. Honda, O. Kitao, H. Nakai, T. Vreven, K. Throssell, J.A. Montgomery Jr, J.E.. Peralta, F. Ogliaro, M.J. Bearpark, J.J. Heyd, E.N. Brothers, K.N. Kudin, V.N. Staroverov, T.A. Keith, R. Kobayashi, J. Normand, K. Raghavachari, A.P. Rendell, J.C. Burant, S.S. Iyengar, J. Tomasi, M. Cossi, J.M. Millam, M. Klene, C. Adamo, R. Cammi, J.W. Ochterski, R.L. Martin, K. Morokuma, O. Farkas, J.B. Foresman, D.J. Fox, Gaussian 16 Rev. C.01, Wallingford, CT, 2016.
[17] Y. Zhao, D.G. Truhlar, A new local density functional for main-group thermochemistry, transition metal bonding, thermochemical kinetics, and noncovalent interactions, J. Chem. Phys. 125 (2006), 194101.
[18] F. Weigend, R. Ahlrichs, Balanced basis sets of split valence, triple zeta valence and quadruple zeta valence quality for H to Rn: Design and assessment of accuracy, Phys. Chem. Chem. Phys. 7 (2005) 3297–3305.
[19] I. Demiroglu, K. Yao, H.A. Hussein, R.L. Johnston, DFT global optimization of gas-phase subnanometer Ru–Pt clusters, J. Phys. Chem. C 121 (2017) 10773–10780.
[20] F. Aguilera-Granja, L.C. Balbás, A. Vega, Study of the structural and electronic properties of RhN and RuN Clusters ($N < 20$) within the density functional theory, J. Phys. Chem. 113 (2009) 13483–13491.
[21] A.M. Abdel-Mageed, B. Rungtaweevoranit, M. Parlinska-Wojtan, X. Pei, O. M. Yaghi, R.J. Behm, Highly active and stable single-atom Cu catalysts supported by a metal–organic framework, J. Am. Chem. Soc. 141 (2019) 5201–5210.
[22] J. Guo, P.N. Duchesne, L. Wang, R. Song, M. Xia, U. Ulmer, W. Sun, Y. Dong, J.Y. Y. Loh, N.P. Kherani, J. Du, B. Zhu, W. Huang, S. Zhang, G.A. Ozin, High-performance, scalable, and low-cost copper hydroxyapatite for photothermal $CO_2$ reduction, ACS Catal. 10 (2020) 13668–13681.
[23] D. Mateo, J. Albero, H. García, Titanium-perovskite-supported $RuO_2$ nanoparticles for photocatalytic $CO_2$ methanation, Joule 3 (2019) 1949–1962.
[24] S. Luo, X. Ren, H. Lin, H. Song, J. Ye, Plasmonic photothermal catalysis for solar-to-fuel conversion: current status and prospects, Chem. Sci. 12 (2021) 5701–5719.
[25] M. Kitano, Y. Inoue, H. Ishikawa, K. Yamagata, T. Nakao, T. Tada, S. Matsuishi, T. Yokoyama, M. Hara, H. Hosono, Essential role of hydride ion in ruthenium-based ammonia synthesis catalysts, Chem. Sci. 7 (2016) 4036–4043.
[26] S.E. Siporin, R.J. Davis, Use of kinetic models to explore the role of base promoters on Ru/MgO ammonia synthesis catalysts, J. Catal. 225 (2004) 359–368.
[27] J.A. Maguire, W.T. Boese, M.E. Goldman, A.S. Goldman, Mechanism of the photochemical dehydrogenation and transfer-dehydrogenation of alkanes catalyzed by trans-$Rh(PMe_3)_2(CO)Cl$, Coord. Chem. Rev. 97 (1990) 179–192.

[28] P. Broqvist, L.M. Molina, H. Grönbeck, B. Hammer, Promoting and poisoning effects of Na and Cl coadsorption on CO oxidation over MgO-supported Au nanoparticles, J. Catal. 227 (2004) 217–226.
[29] S. Murata, K.-I. Aika, Removal of chlorine ions from Ru/MgO catalysts for ammonia synthesis, Appl. Catal. A-Gen. 82 (1992) 1–12.
[30] K.-i Aika, Role of alkali promoter in ammonia synthesis over ruthenium catalysts—Effect on reaction mechanism, Catal. Today 286 (2017) 14–20.
[31] Y.V. Larichev, B.L. Moroz, E.M. Moroz, V.I. Zaikovskii, S.M. Yunusov, E. S. Kalyuzhnaya, V.B. Shur, V.I. Bukhtiyarov, Effect of the support on the nature of metal-promoter interactions in Ru-$Cs^+$/MgO and Ru-Cs+-$Al_2O_3$ catalysts for ammonia synthesis, Kinet. Catal. 46 (2005) 891–899.
[32] Y. Baik, M. Kwen, K. Lee, S. Chi, S. Lee, K. Cho, H. Kim, M. Choi, Splitting of hydrogen atoms into proton–electron pairs at BaO–Ru interfaces for promoting ammonia synthesis under mild conditions, J. Am. Chem. Soc. 145 (2023) 11364–11374.
[33] H.V. Thang, S. Tosoni, L. Fang, P. Bruijnincx, G. Pacchioni, Nature of sintering-resistant, single-atom Ru species dispersed on zirconia-based catalysts: a DFT and FTIR study of CO adsorption, ChemCatChem 10 (2018) 2634–2645.
[34] E. Guglielminotti, F. Boccuzzi, M. Manzoli, F. Pinna, M. Scarpa, Ru/$ZrO_2$ catalysts: I. O2, CO, and NO adsorption and reactivity, J. Catal. 192 (2000) 149–157.
[35] M. Weber-Stockbauer, O.Y. Gutiérrez, R. Bermejo-Deval, J.A. Lercher, Cesium induced changes in the acid–base properties of metal oxides and the consequences for methanol thiolation, ACS Catal. 9 (2019) 9245–9252.